



# Detection and assessment of flaws in friction stir welded joints using ultrasonic guided waves: experimental and finite element analysis



Mohammad Ali Fakh<sup>a</sup>, Samir Mustapha<sup>a,\*</sup>, Jaafar Tarraf<sup>a</sup>, Georges Ayoub<sup>b</sup>, Ramsey Hamade<sup>a</sup>

<sup>a</sup> Department of Mechanical Engineering, Maroun Semaan Faculty of Engineering and Architecture, American University of Beirut, Beirut, Lebanon

<sup>b</sup> Industrial and Manufacturing Systems Engineering Department, University of Michigan Dearborn, 48128 Dearborn, MI, USA

## ARTICLE INFO

### Article history:

Received 16 December 2016

Received in revised form 20 July 2017

Accepted 2 September 2017

### Keywords:

Lamb waves

Weld inspection

Structural health monitoring

Friction stir welding

CT scanning

Finite element analysis

## ABSTRACT

Ultrasonic guided waves (GWs), e.g. Lamb waves, have been proven effective in the detection of defects such as corrosion, cracking, delamination, and debonding in both composite and metallic structures. They are a significant tool employed in structural health monitoring.

In this study, the ability of ultrasonic GWs to assess the quality of friction stir welding (FSW) was investigated. Four friction stir welded AZ31B magnesium plates processed with different welding parameters and a non-welded plate were used. The fundamental symmetric ( $S_0$ ) Lamb wave mode was excited using piezoelectric wafers (PZTs). Further, the  $S_0$  mode was separated using the “Improved complete ensemble empirical mode decomposition with adaptive noise (Improved CEEMDAN)” technique. A damage index (DI) was defined based on the variation in the amplitude of the captured wave signals in order to detect the presence and assess the severity of damage resulting from the welding process. As well, computed tomography (CT) scanning was used as a non-destructive testing (NDT) technique to assess the actual weld quality and validate predictions based on the GW approach. The findings were further confirmed using finite element analysis (FEA).

To model the actual damage profile in the welds, “Mimics” software was used for the 3D reconstruction of the CT scans. The built 3D models were later used for evaluation of damage volume and for FEA. The damage volumes were correlated to the damage indices computed from both experimental and numerical data.

The proposed approach showed high sensitivity of the  $S_0$  mode to internal flaws within the friction stir welded joints. This methodology has great potential as a future classification method of FSW quality.

© 2017 Elsevier Ltd. All rights reserved.

## 1. Introduction

Friction stir welding (FSW) is recognized as a novel, environmentally friendly, solid state welding process [1] that was invented and validated by W. Thomas and his colleagues at The Welding Institute in the UK in 1991 [2,3]. It is being widely used in the automotive, aerospace, and naval industries. The welding process is carried out at a temperature below the melting points of the welded metals [4,5]. The metal is thereby exposed to minimal heat, leading to many advantages such as

\* Corresponding author.

E-mail address: [sm154@aub.edu.lb](mailto:sm154@aub.edu.lb) (S. Mustapha).

good steadiness of dimensions, control of weld quality, exceptional mechanical properties of the weld zone, reduction of porosity and solidification cracking, minimization of the need for surface cleaning, and reduction of environmental impact [1,6]. FSW is carried out using a non-consumable rotating cylindrical tool with a shoulder and a pin. The pin is inserted into the adjacent edges of the sheets/plates to be joined, then translated along the line of the joint. The pin is slightly shorter than the required weld depth, and the shoulder is pushed down on the plates' surfaces, causing a high frictional force while rotating. As a result, the tool provides the heating to the workpiece and further ensures the flow of the material to produce the joint.

Several disadvantages, though not major, are associated with this welding technique; they include the hole that is left behind when the tool is withdrawn from the workpiece, the need for a large downward force, and the constraints on the possibility of generating different weld profiles – although the latter may not be a major issue with the advances in robotic systems and automation [7].

The spindle speed and the tool feed both influence the quality of the produced weld, besides other variables such as the tool geometry, the tool materials, and the sheet materials. Optimizing the welding parameters is crucial to reduce surface and internal defects and hence increase the integrity of the weld. Much research effort over the years has focused on improvement of the microstructure in FSW joints, in particular, reducing the intermetallic phase and characterizing the grain size and hardness of the mixed materials at the interface. These efforts have further led to optimization of the welding process parameters and have engendered interest in the research community to improve the FSW process of bimetallic structures [8–13].

Inappropriate selection of welding parameters during the FSW process can cause one or several types of defect within the welded zone, such as worm hole, scalloping, ribbon flash, surface lack of fill, nugget collapse, and surface galling, as indicated in Fig. 1 [14]. Thus, quality inspection of the resulting weld is a necessity to ensure adequate performance during service. Internal defects (e.g. worm holes) are usually difficult to detect, therefore, weld inspection requires the use of either destructive or advanced techniques. Moreover, monitoring the quality of welds is essential for detecting and correcting any variation in the weld conditions or for recalibrating the welding parameters when needed.

Various NDT methods are currently available for quality control of welds, including visual inspection, acoustic emission, eddy-current, and ultrasonic inspection. Visual inspection is limited to surface defects, and the other techniques can only provide local evaluation of a specific region on the structure. These techniques are labor intensive, costly, and time-consuming when used for inspecting large structures. They also require experienced personnel and, most importantly, cannot be performed without disrupting the functionality of the inspected structure [15].

GWs have been proposed as an essential tool to be implemented in SHM systems in order to provide continuous monitoring of metallic and composite structures due to their ability to propagate for long distances in simple and complex

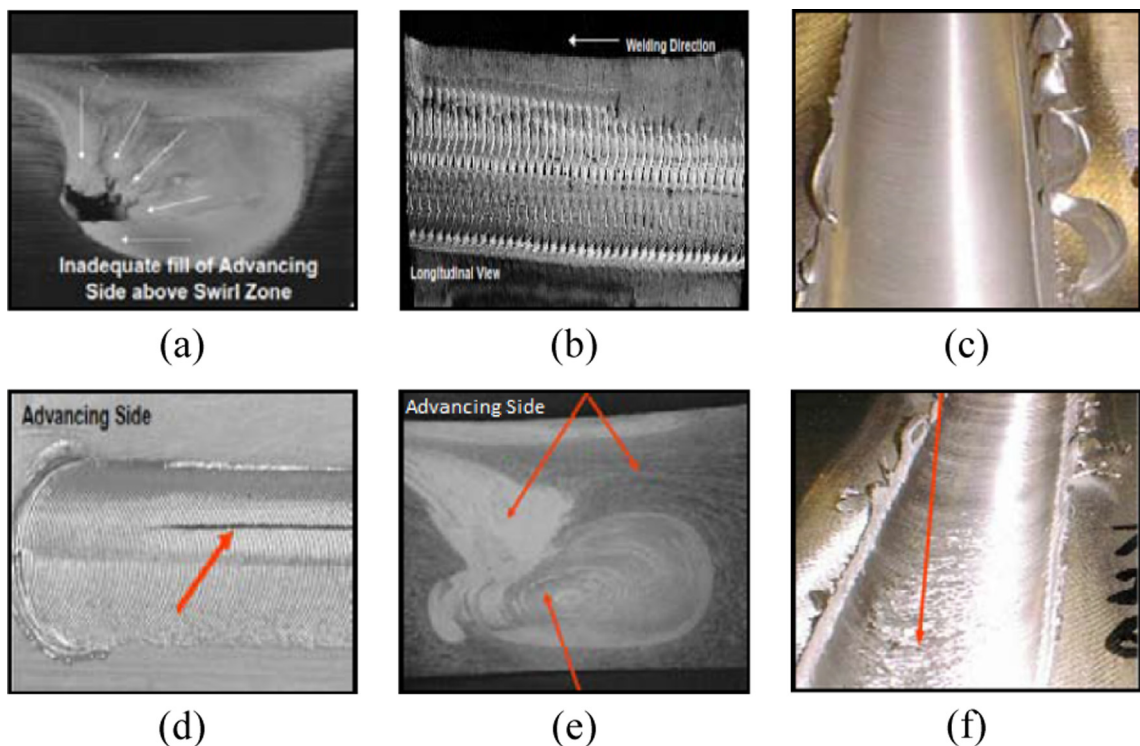


Fig. 1. FSW defects, (a) to (f): worm hole, scalloping, ribbon flash, surface lack of fill, nugget collapse, and surface galling [14].

curvatures. GWs, in particular Lamb waves, have very high sensitivity to surface and internal cracking, that is due mainly to the propagation behavior of the fundamental anti-symmetric ( $A_0$ ) and symmetric ( $S_0$ ) modes and high order modes within the inspected structure [16]. Over the last decades, the proficiency of Lamb waves has been proven, and they have been widely used to develop damage identification algorithms for assessing fatigue cracking, delamination, fiber breakage, debonding holes, cracks/notches, and corrosion in composite and metallic plate-like structures [17–24].

The use of ultrasonic waves for weld inspection has also been investigated to some extent, but research has focused mainly on arc welding, with only few studies focusing on FSW. In 1986, Burch et al. [25] used pulse-echo multi-angle ultrasound scanning to detect and classify various types of hidden weld defects in ferritic steels. They established physical models of ultrasound interaction with such kinds of defect, choosing damage sensitive features to develop an automated classifier. In 1992, Karim et al. [26] studied the scattering behavior of elastic waves in a plate containing inclusions and/or cracks, based on numerical and analytical analyses. The effects of different types of inclusions and crack shapes and sizes were investigated. Further, they considered welds in aluminum plates and found that welds resulted in greater reduction in the magnitude of the displacement spectra in the horizontal direction than in the direction normal to the surface. In 1999, Dixon et al. [27] proposed a combined laser-electromagnetic acoustic transducer (EMAT) system for weld examination. Large amplitude ultrasonic waves were generated in samples by illuminating the surface with a laser beam using a pulsed laser, and EMAT was used as the receiver. The authors compared the B-scans and reflections and conversions of wave modes between a blank steel plate and weld-defected plates to identify the existence and location of damage. They suggested that the system could be suitable for a quick pre-screening inspection, because it was not sensitive to all types and sizes of defect. Kažys et al. [28] studied the interaction between GWs and welds or other irregularities in liquid-loaded steel plates as tank floors. Based on their experimental and numerical analysis, the authors concluded that a defect or a weld reflected acoustic energy into the liquid which could later be captured and used for detection of flaws. On the other hand, Arone et al. [29] made use of both non-contact pulsed laser and contact angle-beam actuators to excite ultrasonic waves in aluminum welded joints. The two types of waves were received by an air-coupled sensor and were used to locate and characterize defects respectively. Later, Lu et al. [30] investigated the use of Lamb waves induced and sensed using PZTs to detect and localize welds, cracks, and cracks containing different types of impurity within steel plates. The authors compared the peak-to-peak amplitudes of the incident and damage-reflected waves to identify the defects. They used several signal processing and pattern recognition techniques, namely wavelet transform (WT), continuous WT, and Hilbert transform, to improve the damage detection process. As well, numerical simulation was used for validation. Moreover, Yang et al. [31] have proposed a Bayesian-based probabilistic approach for the quantification of crack size using Lamb waves in 2024-T3 aluminum plates. The waves were excited and captured using piezoelectric wafers in a pitch/catch configuration. Phase change and the normalized amplitude of the  $S_0$  mode were used as damage sensitive features, and they established a predictive model which has the flexibility of being updated based on the data coming from the monitored structure.

Further processing techniques such as wavelet package analysis in time-frequency domain, and learning techniques such as classification and regression tree (CART) and random forest, were also applied on ultrasonic data for the assessment of the quality of resistance spot welding [32,33].

Santos et al. [34] investigated the ability of Lamb waves to assess FSW in aluminum plates and compared the results to weld qualities obtained through X-ray and C-scan inspection methods. They used a pitch-catch configuration while the specimen was submerged in a water medium. The authors argued that their proposed technique is efficient in providing a qualitative classification of linear FSW in aluminum plates. On the other hand, the technique lacked the ability to detect miniature weld flaws.

In a recent study, Tabatabaeipour et al. [35] used an immersion setup and a pitch-catch technique to capture nonlinear features that were generated in the reflected signals due to FSW kissing bond defects. The authors used Fermat design transducers to focus and receive ultrasonic shear waves in aluminum welded plates. The signals were then analyzed using pulse inversion, and the results were validated numerically and experimentally. A Fermat surface of a transducer is the surface where the travel time of the wave is the same from any point on this surface to the point intended to be focused on; hence the Fermat transducer design depends on the tested material and its thickness. Further, Tabatabaeipour et al. [36] used an angle-beam technique for ultrasonic inspection of friction stir welded aluminum butt-joints, also in an immersion setup. After scanning the whole weld in the cross-sectional and longitudinal directions, they managed to detect and qualitatively identify the type and severity of root flaws by inspecting the backscattered energy from the underside of the weld.

NDT techniques that require a structure to be totally immersed in water when inspection is needed lack the flexibility to be integrated in SHM systems that eventually aim to provide continuous monitoring.

This study focuses on the development of an ultrasonic guided wave (Lamb waves) based method for weld inspection, with particular interest in friction stir welds. An assessment approach originating from the mode separation using Improved CEEMDAN is proposed for assessing the quality of FSW in AZ31B magnesium alloy plates. Different weld qualities are achieved by varying the weld parameters, in this case the pin insertion depth. Later, Lamb waves are actuated and captured using PZT ceramics. Signal processing using the Improved CEEMDAN approach is applied to separate the fundamental  $S_0$  mode and a DI is calculated based on the amplitude variation of the wave transmitted through the welded and the non-welded plate. The resulting DIs are correlated with the actual damage volumes determined from the CT images of the plates. The results are also validated using FEA.

## 2. Experimental setup

Two PZTs (PI Ceramics, Lederhose, Germany) 10 mm in diameter and 1 mm in thickness, spaced 90 mm from each other, were mounted on either side of the weld on each of the tested specimens. One PZT wafer functioned as an actuator while the other served as a sensor. Five sinusoidal cycles in a Hanning window, at frequencies of 200, 250, 300, 350, and 400 kHz, were generated at a sampling rate of 20 MSa/s, and amplified to 60 V peak-to-peak using an amplifier (EPA-104 Linear Amplifier, Piezo Systems Inc.). The generated cycles were fed into the actuator PZT using an arbitrary waveform generator (33500B Series Waveform Generator, Keysight Inc.). A high-rate acquisition oscilloscope (InfiniiVision DSO-X 3024 Digital Storage Oscilloscope, Keysight Inc.) was employed to capture the wave signals from both the actuator and the sensor. Fig. 2 illustrates the experimental setup.

Four plates of various weld qualities were produced by varying one of the FSW process parameters, i.e. the pin insertion depth, and a fifth non-welded plate was used for comparison. The material of the tested plates was AZ31B magnesium alloy. Each plate was 100 mm long, 100 mm wide, and 3 mm thick. All welds were accomplished with a turning speed of 1200 RPM and an advancing speed of 150 mm/h, while the pin insertion depth was varied as listed in Table 1. The welded plates were randomly named as Plate 1 to Plate 4 and the non-welded plate was named as Plate 0. Fig. 3 shows all the plates with their corresponding numbers. The plates were simply supported on Plexiglass supports that were in turn fixed to a damping table.

## 3. CT scans

The five specimens were scanned using a high-resolution CT scanner (Philips Brilliance iCT 256) with a pixel size down to 0.335 mm. The CT images of the specimens were used to identify the imbedded defects through the welds and quantify the weld qualities in the tested specimens. Further, a 3D model was constructed based on the CT images, that was used later for FEA toward the validation of the experimental results.

It was recognized that the welded plates contained worm holes, but of different sizes and shapes. Fig. 4 shows all the plates, with the order described earlier maintained. Each plate is shown in two cross-sectional views, one section perpendicular to the weld direction and in the middle of the plate where the PZTs were placed, the other section parallel to the

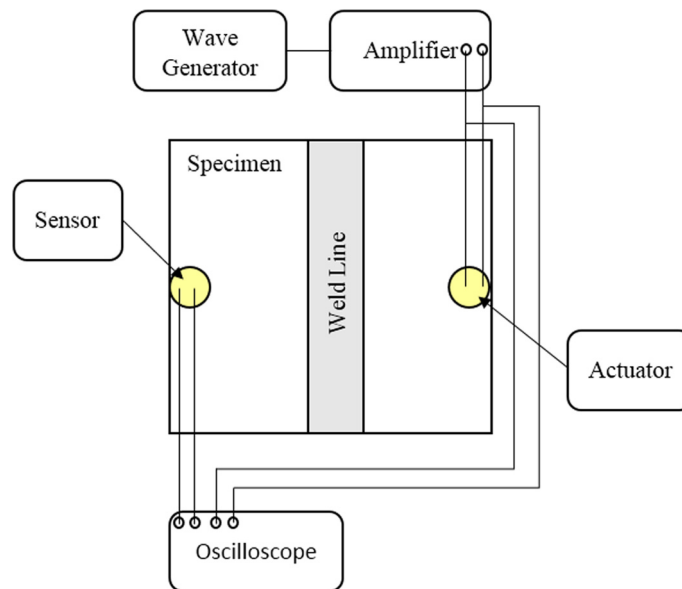
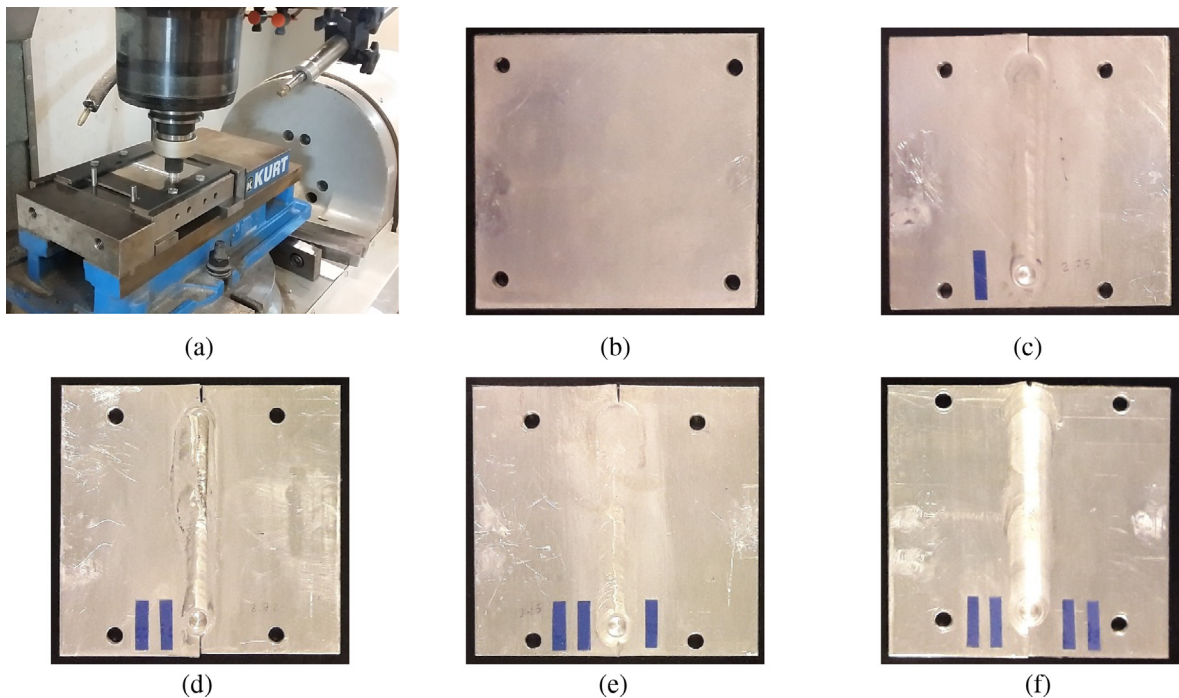


Fig. 2. Schematic of the experimental setup.

Table 1  
Specimens weld parameters.

Plate number	Rotational speed (RPM)	Transversal speed (mm/h)	Pin insertion (mm)
0	No weld	No weld	No weld
1	1200	150	2.75
2	1200	150	2.725
3	1200	150	2.85
4	1200	150	2.87



**Fig. 3.** (a) A photo of the friction stir welding process and the used fixture, (b) to (e) the tested plates named Plate 0 to 4.

surface of the plate and passing through the worm hole in its widest section. Plate 0 containing no weld is also shown to confirm the continuity in the raw material and the high quality of the CT scans.

Based on the information provided by the CT scans, the specimens were arranged in descending order in terms of their weld quality, starting with Plate 0 (with no weld), Plate 4, Plate 3, Plate 1, and finally mPlate 2, that was the most damaged plate.

#### 4. Construction of 3D models and FEA

In this section, the construction of the finite element models based on the CT scans is described. “Mimics Research 18.0” (Materialise, Ann Arbor, Michigan, USA) was used to convert the CT scans (DYCOM format) into 3D models. The procedure flowed as follows after importing the CT scans:

- Create a mask through the selection of upper and lower grayscale thresholds of the pixels within the region of interest.
- Each slice in the mask is cleaned to eliminate blurry pixels or those pixels that do not belong to the plate.
- Create two additional masks to define the location of the actuator and the sensor.
- Create a voxel mesh from the combined masks (defined in the steps above) and export it as an input file.

Fig. 5 shows the voxel mesh obtained for Plate 1. Post the friction stir welding process, notches appear at the non-welded ends of the weld line as shown in Fig. 5. Since the coverage of the propagating wave (between the transmitter and the receiver) will not reach the extreme ends of the plates, where the notches were located, hence removing the notches will have no significant effect on the contents of the waves. Therefore, the edges in the 3D model were straightened while maintaining the critical information related to the plate dimensions, thus the spacing between the PZT wafers.

The elements of the voxel mesh were chosen to be hexahedral 8-point elements, and each voxel mesh contained an average of 421,476 elements and 474,974 nodes.

The excessive deformation from the friction stir welding process, appeared to impact the micro-structure and therefore the yield strength and hardness of the material in the weld zone [37]. However, it was shown that the elastic properties remain unaffected and do not vary from those of the base metal. Dorbane et al. [37] worked on the characterization of AZ31B magnesium alloy friction stir welded joints, the welded zone and the base metal were shown to have the same elastic modulus. This can be observed in the stress-strain curves published by the authors and determined at room temperature. A similar conclusion was also made from the stress-strain curves shown in [38] for AZ31B base metal and friction stir welded samples.

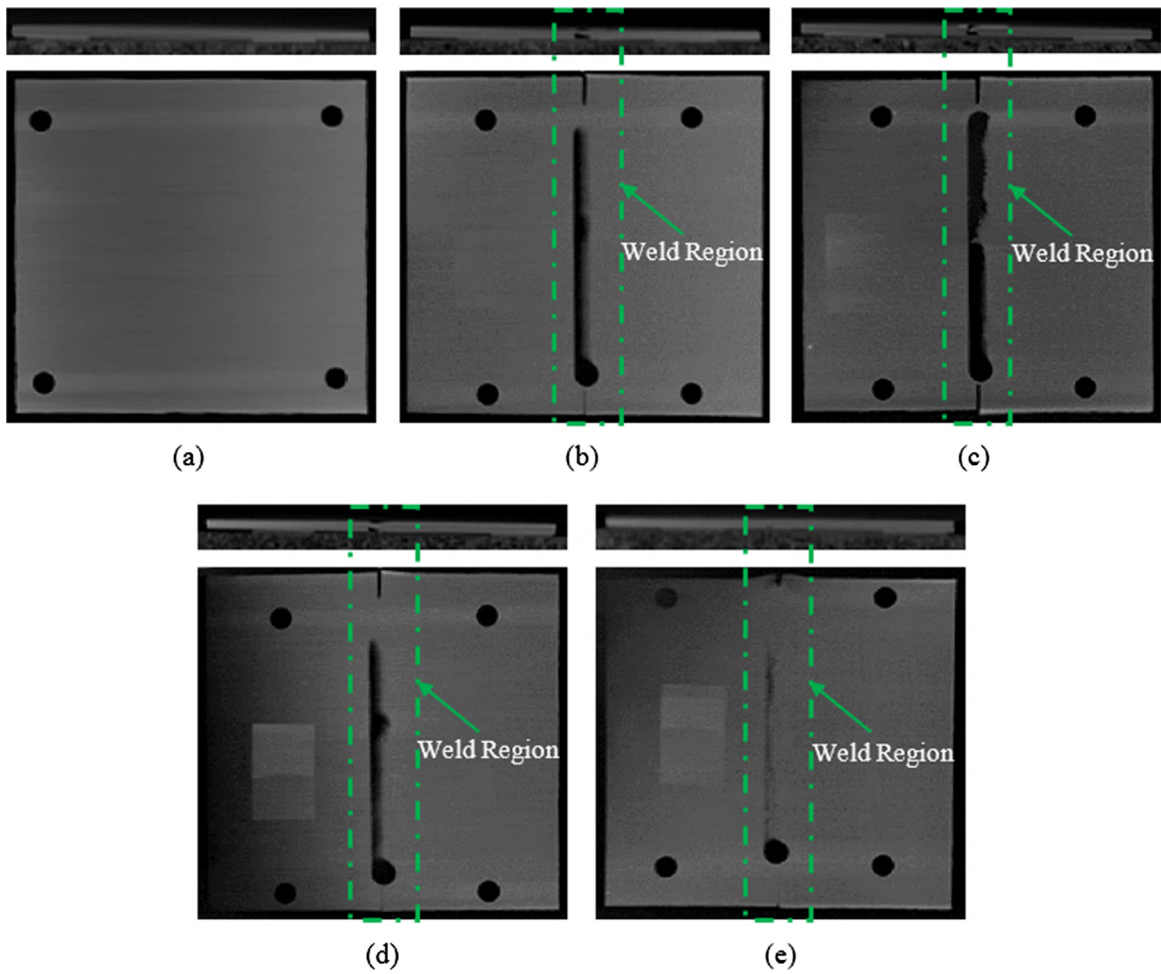


Fig. 4. Cross-sectional views: (a) to (e) corresponding to Plates 0 to 4, respectively.

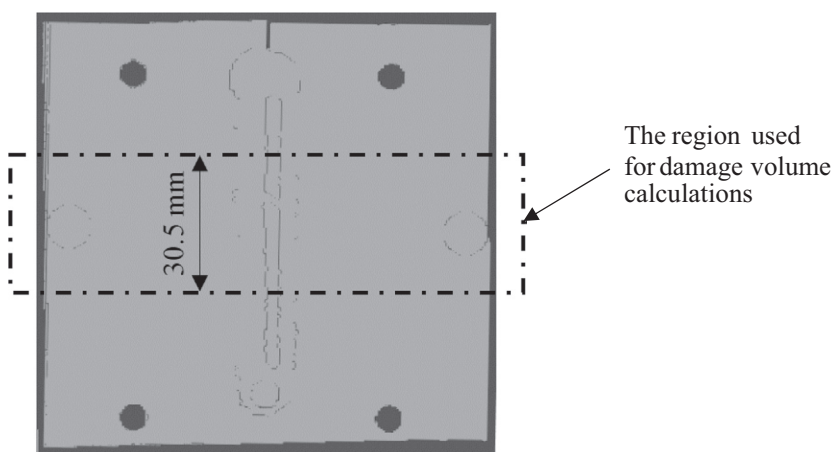


Fig. 5. The voxel mesh of Plate 1 created using Mimics.

Hence, after the 3D models had been created, the input files were imported into “Abaqus 6.14” and were assigned the elastic material properties of AZ31B magnesium alloy ( $\rho = 1.77 \text{ g/cm}^3$  [39],  $E = 44.8 \text{ GPa}$  [40], and Poisson’s ratio  $\nu = 0.35$  [40]).

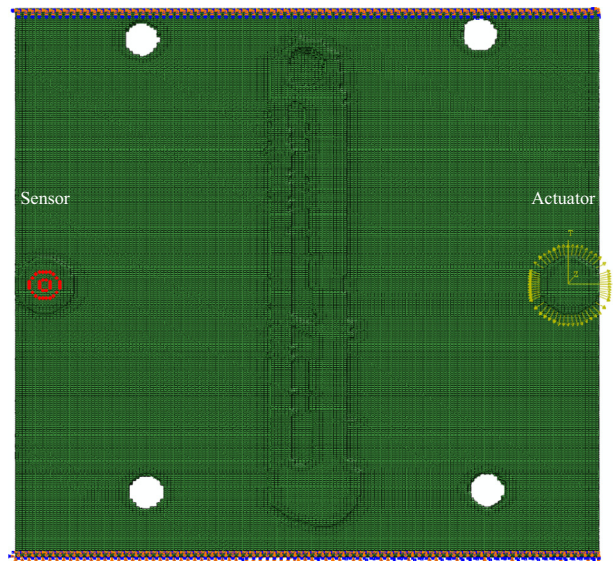


Fig. 6. Illustration of the sensing nodes, boundary conditions, and actuator loading in the finite element model.

The mesh created in “Mimics” is imported into “Abaqus” as an orphan mesh and therefore the mesh remained the same. Thus, the finite element model of each plate was composed of linear hexahedral elements of type C3D8, with an average of 421,476 elements and 474,974 nodes, leading to a total of 1,424,922 degrees of freedom per model. Upon meshing using “Mimics”, the resolution of the performed CT scans allowed for an average element size of about  $0.58 \times 0.34 \times 0.34 \text{ mm}^3$ . Consequently, nine elements were obtained across the 3-mm thickness of the plate. Moreover, since the wavelengths of the excited wave modes ranged between 9.12 mm and 42.675 mm, more than 10 elemental nodes per wavelength were available, which obeys the recommended element size for the excitation of Lamb waves using FEA [41].

Lamb waves were excited by prescribing concentrated forces along the nodes of the PZT element, as in the actuator model shown in Fig. 6 in the case of a circular shaped PZT. The edges perpendicular to the weld direction were simply supported to emulate the boundary conditions of the experimental setup. The simulated Lamb signals were acquired using a sensor model [23] at the rate of 20 MHz. Fig. 6 shows an example of the loading (the yellow arrows on the right PZT), sensing nodes (the nodes in red on the left PZT), and the boundary conditions (on the upper and lower edges) used for one of the plates (Plate 1). The analysis was performed using the dynamic explicit solver with a maximum time step of  $5e^{-8}$  s over a total period of 0.1 s for each simulation.

## 5. Signal processing

Selection of the wave mode is critical, considering the importance of the mode sensitivity to the type of damage of interest. For this purpose, a Matlab based software “Wavescope”, developed by the Laboratory for Active Materials and Smart Structures (LAMSS) [42], was used. The group velocities, wavelengths, and strains plots were generated for the  $S_0$  and  $A_0$  wave modes (for the magnesium AZ31B alloy plates). This helped to identify and evaluate the possible wave modes in the structure, that were suitable for this application. Figs. 7 and 8 show respectively the results given by “Wavescope” for the expected group velocities and strains of different Lamb wave modes in AZ31B magnesium alloy [42]. Further, the strains shown in Fig. 8 provide prior knowledge about the dominant modes at each of the selected frequencies. Based on the above results, the five frequencies of 200, 250, 300, 350, and 400 kHz were chosen to excite only the fundamental  $A_0$  and  $S_0$  modes.

After the experimental response waveforms had been obtained from the sensors, an analysis of the raw data was performed based on the first wave pack transmitted. The positions of the highest peaks of the first wave packs were compared to those of the highest peaks of the inputs in order to calculate the velocities of the observed wave modes. Velocities were compared to those predicted by “Wavescope” to identify the modes in the first transmissions. As an example, Fig. 9 shows the normalized input and output signals sensed from Plate 0 at an excitation frequency of 200 kHz. The dotted curve corresponds to the normalized input signal and the solid line corresponds to the normalized output signal. Once the time of flight was determined, the velocity could be calculated according to Eq. (1):

$$V_{200} = \frac{\text{Distance between the actuator and sensor PZTs}}{\text{Time difference between the peaks}} = \frac{0.09}{(3.12e^{-5} - 6.3e^{-6})} = 3614.46 \text{ m/sec} \quad (1)$$

According to “Wavescope”, the expected group velocity of the  $S_0$  mode at 200 kHz was 5268 m/s and that of the  $A_0$  mode was 2962 m/s. Due to the disturbed raw experimental signals, the experimentally calculated velocity ( $V_{200}$ ) did not match

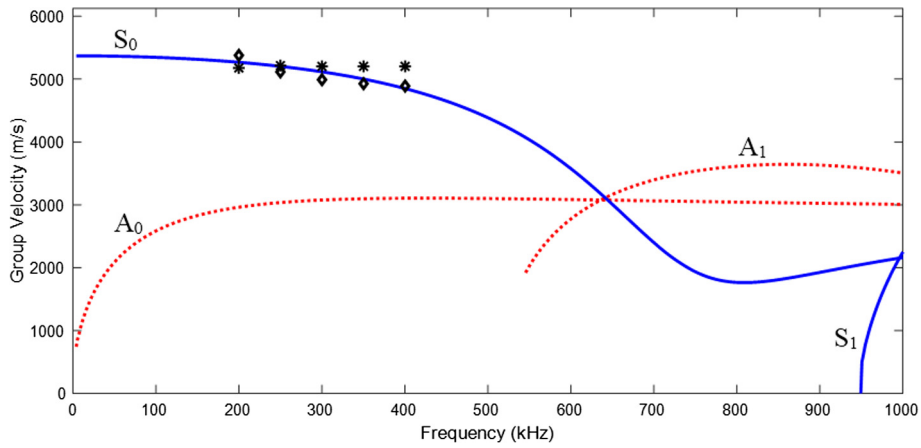


Fig. 7. Analytical group velocities of the first four Lamb wave modes in AZ31B magnesium alloy along with the obtained experimental ' $\diamond$ ' and FEA '\*' results.

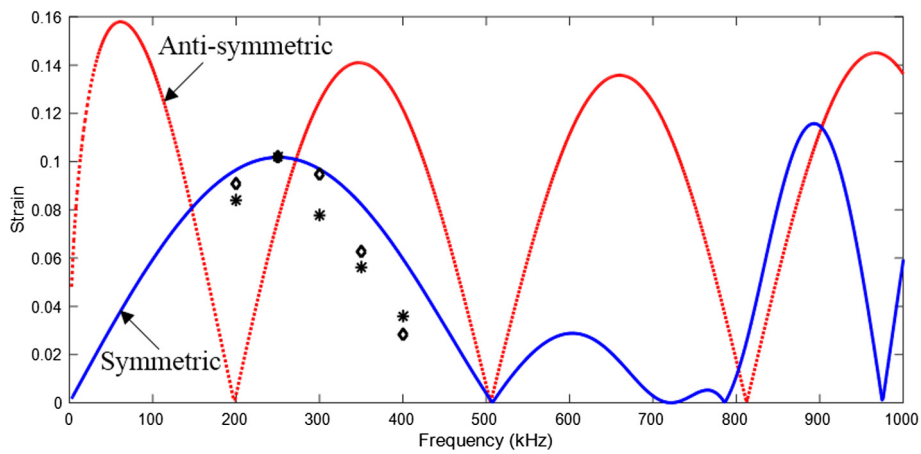


Fig. 8. Analytical strain values of the symmetric and anti-symmetric Lamb wave modes in AZ31B magnesium alloy along with the obtained experimental ' $\diamond$ ' and FEA '\*' results.

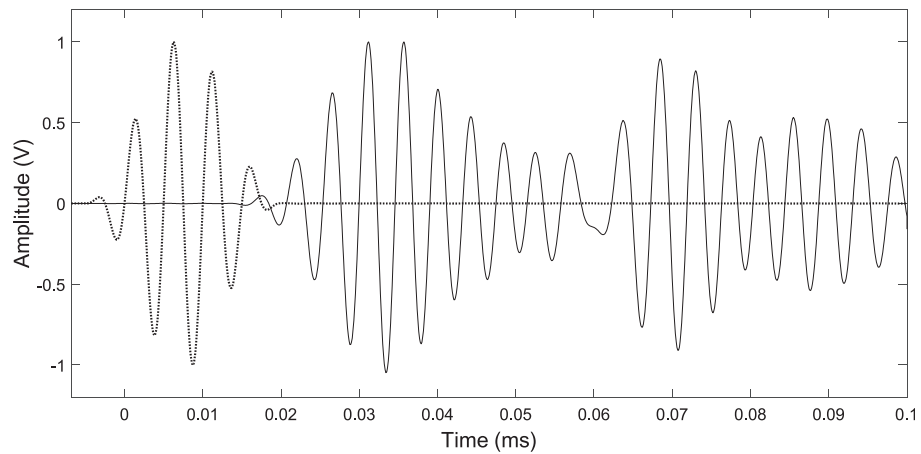


Fig. 9. Captured wave signal at an excitation frequency of 200 kHz; the dotted line is the normalized actuator and the solid line is the normalized sensor.

either of the two “Wavescope” values. Although the first transmission should be the  $S_0$  mode because it is the fastest mode, the highest peak in the first transmission did not seem to correspond to  $S_0$ .

The disturbance of the raw signals was caused by their superposition with their reflections from the boundaries of the plates. This was due to the fact that Lamb waves propagate at very high velocities in metals, and because of the small size of the tested specimens. Consequently, the sensed waveforms did not show clear mode separation, and complex signals were observed. Therefore, direct use of the peak amplitude and time of arrival might not be immediately feasible. On this basis, the Improved CEEMDAN method for mode separation was adopted and is described in the Section 6.

Post the separation, the group velocities and the normalized amplitudes of the  $S_0$  mode, at the selected excitation frequencies, are presented in Figs. 7 and 8, respectively. The experimental values of the group velocities correlated well with the analytical output from “Wavescope”. Further, the numerical values were observed to be slightly higher than the experimental results. On the other hand, the strain values resulting from the experimental and numerical studies were shifted down from the analytical values, however, they all maintained the same trend with maximum strain values recorded at the excitation frequency of 250 kHz.

## 6. Improved CEEMDAN technique

Ng [43] has presented a comparative study of several signal processing techniques for GW damage identification. The compared techniques were fast Fourier transform, Hilbert transform, and two time–frequency resolution methods (TFRs), namely, Gabor wavelet transform and discrete wavelet decomposition. Comparison was based on the accuracy and uncertainty of the methods when applied on GW responses to predict the location and dimensions of damage *when combined with a statistical damage identification framework*. Gabor wavelet transform was proved to be superior to the other compared approaches, however, in traditional linear TFRs such as short time Fourier transform and WT, care should be given to the choice of a previously defined window or a base function before applying the technique. Unlike those methods, empirical mode decomposition (EMD) is totally driven by the data itself. This gives EMD the ability to deal with nonlinear and non-stationary signals [44].

Moreover, conventional TFRs, in general, do not have the potential of separating overlying multimodal wave packets, while TFRs that have a superior resolution potential are known to be computationally expensive [45]. The Improved CEEMDAN technique was proved, in this work, to have the ability of separating overlapping multimodal responses in a computationally effective manner. The proposed signal decomposition and its post processing, e.g. choosing and processing the relevant decomposed mode, can be easily employed in a fully automated process. Those advantages in addition to its robustness to noise and adaptivity to the decomposed signal [46] make it a suitable choice for implementation in real-world online SHM applications.

EMD is a well-known signal-adaptive separation method, first proposed by Huang et al. [44]. Subsequently, a series of improvements and adaptations were suggested by several authors to overcome the disadvantages of EMD, as well as those of the attempted improvements, such as mode mixing, residual noise, incompleteness, late appearance of the signal information in the modes, and reconstruction errors. Trials of improvements included ensemble EMD (EEMD) [47], complementary EEMD [48], complete EEMD with adaptive noise (CEEMDAN) [49], and Improved CEEMDAN [46].

EMD expresses a signal as a totality of amplitude and frequency modulated (AM–FM) functions called “intrinsic mode functions” (IMFs), or modes, plus a last monotonic trend. An IMF signal is defined as a signal having: (1) its number of zero crossings the same as its number of extrema (maxima and minima) or varying just by 1, and (2) the mean of its lower and upper envelopes, called local mean, equal to zero [46].

Improved CEEMDAN was proposed by Colominas et al. [46], and it showed robust separation results with minimum residual errors in comparison to its predecessors. The approach divides the complex signal into several amplitude and frequency modulated functions called modes, where the sum of those modes will rebuild the original signal with a negligible residual error [46]. The EMD and the Improved CEEMDAN algorithms are given in the appendix of this paper for completeness.

Improved CEEMDAN creates a chosen number of noisy realizations of the original signal and calculates the local mean of each. After that, the average of the local means is subtracted from the original signal to yield the first mode and then the procedure is repeated on the remainder, providing more modes until the remainder satisfies a certain stopping criterion.

The algorithm is described in the flowchart in Fig. 10. Please refer to the appendix for a detailed explanation.

Fig. 11 shows the 10 modes obtained by Improved CEEMDAN when decomposing the response signal captured from Plate 0 at an excitation frequency of 200 kHz. The original signal is shown in Fig. 11(a).

By inspecting the order of amplitudes in comparison to the original signal, it was observed that the second and the third modes were the most relevant because they had the highest orders, i.e., they maintained the most information. However, Peng et al. [50] and Ayenu-Prah et al. [51] proposed correlation-based criteria to select the most relevant modes after EMD decomposition. It was also noticed after calculating the correlation between the original signal and the separated modes that the second and third modes had the highest values. Therefore, the correlation between the mode and the original signal was chosen as a criterion to select the relevant modes after the Improved CEEMDAN separation is applied.

The convenience of the second mode was that it had approximately the shape of the input signal, which was a desired result (Fig. 11(c)). Some of the modes in the decomposed signal were separated from each other, but the reflections of the mode itself were very close to the first transmission, as observed in the third mode (Fig. 11(d)). After calculating the

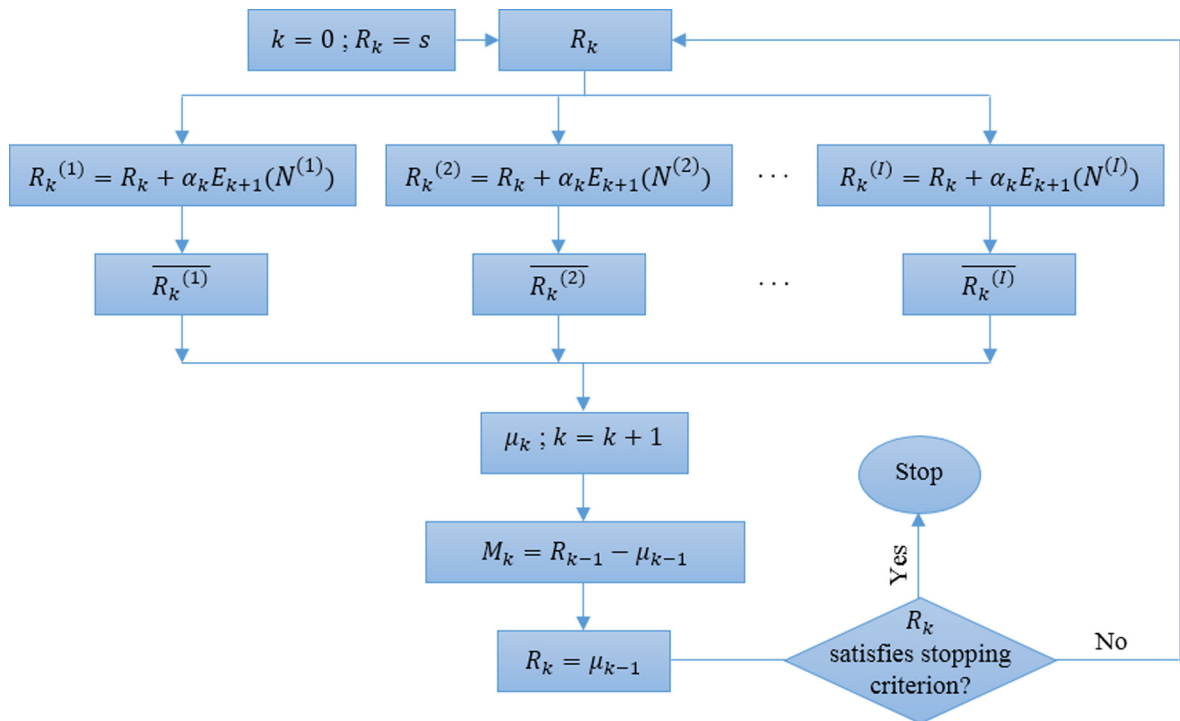


Fig. 10. Flowchart of the algorithm based on the Improved CEEMDAN technique.

velocities of each of those two modes, it was concluded that the second separated mode is the  $A_0$  mode, while the third separated mode is the  $S_0$  mode.

The robustness of the Improved CEEMDAN technique depends on the choice of the chosen number of realizations ( $I$ ) and the signal to noise ratio ( $SNR$ ) of the noise added to those realizations. Different numbers of realizations including 20, 50, 100, 200, 300, 400, 500, and 1000 realizations were tested along with typical  $SNR$  values of 0.1, 0.15, and 0.2.

Experimental and FEA data captured from Plate 0 using the five used excitation frequencies (200, 250, 300, 350, and 400 kHz) were evaluated. Ten trials of separation were performed for each of the used signals and with different parameters' variations (i.e.  $I$  and  $SNR$ ).

As mentioned earlier, the  $S_0$  mode was identified based on its group velocity and its correlation with the original signal. The amplitude of the extracted  $S_0$  mode and its correlation value were determined for each of the combinations considered. The mean amplitude  $A_m$ , the standard deviation  $A_{std}$ , and the mean correlation value of the ten trials of each parameters' combination, were also calculated.

It was observed that the variation of  $A_{std}$  from  $A_m$  is reduced with the increase in the number of realizations for a given  $SNR$ . For instance, taking  $I = 1000$  realizations and  $SNR = 0.15$  for the experimental response of the 300 kHz frequency resulted in a variation of 0.5%, while reducing the  $I$  value to 100 resulted in a minor increase in the variation to 2%. On the other hand, reducing  $I$  further (20 realizations), would result in considerable variations among the 10 trials, which may exceed 5%.

Increasing  $I$  value also increases the elapsed computational time significantly. For instance, the average time for separating a signal excited at 350 kHz using 100 realizations (of the signal) is 21.5 s, using 500 realizations is 110.9 s, and using 1000 realizations is 228.4 s on an "Intel Xeon E5-2650 v3 2.30 GHz" processor. While  $SNR$  value doesn't show any influence on the computational time, the computational time increases linearly with the increase of  $I$ .

Based on the above, the number of realizations selected for the rest of the study was 100 for the purpose of lowering the computational time while keeping a robust separation of the signal. Besides, the correlation between the extracted  $S_0$  mode and the original signal was used to choose the best fitted  $SNR$  value for the separation procedure.

## 7. Results and discussion

### 7.1. Experimental raw data analysis

To identify the weld quality, we used the measured experimental raw data; the Improved CEEMDAN approach for mode separation was not applied. As discussed earlier, the  $S_0$  mode is used to detect internal defects, and its sensitivity to damage

severity is scrutinized. The superposition of multiple wave packs of the excited modes, including the  $S_0$  and  $A_0$  modes, resulted in complex signals. The first captured wave pack was not purely  $S_0$  mode, but a superposition of  $A_0$ ,  $S_0$ , and boundary reflections. Therefore, the front of the wave pack was used to compare the response of the wave signals captured from different plates (i.e. the second cycle of the received wave pack was considered). Table 2 presents the amplitude of the first

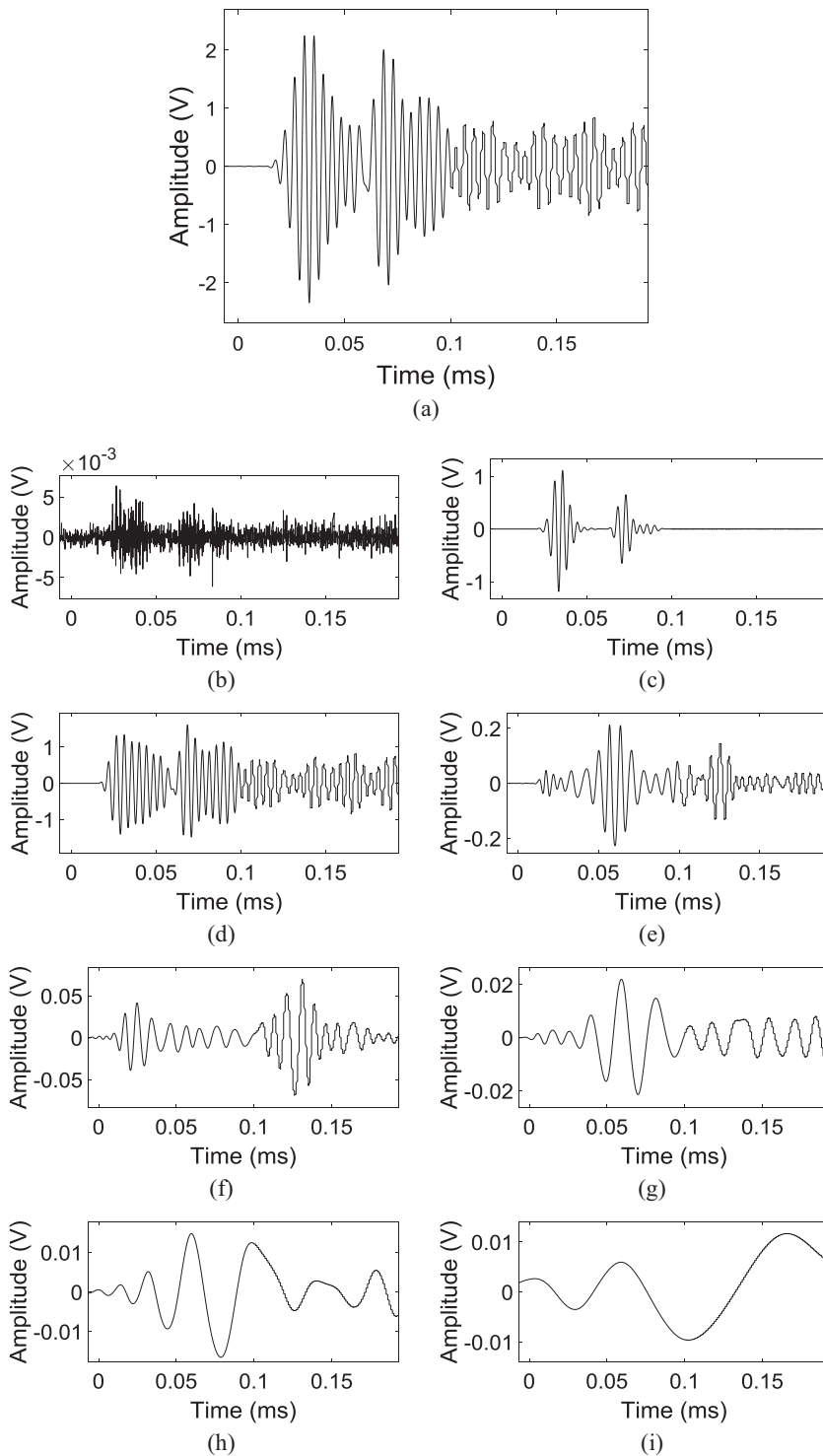


Fig. 11. (a) The original signal excited in mPlate 0 at 200 kHz; (b) to (k) are the 10 modes obtained after the separation of the signal using the Improved CEEMDAN technique.

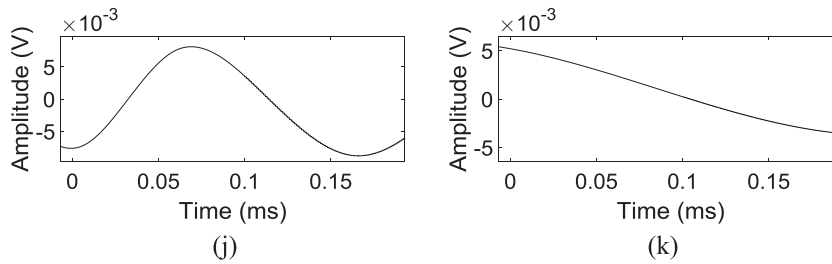


Fig. 11 (continued)

**Table 2**  
Calculated DI based on the raw experimental data.

Frequency (kHz)	Plate number	Transmitted wave signal amplitude (V)	Variation in the transmitted wave signal amplitude (V)	DI
200	0	0.621	0.000	0.000
	4	0.568	0.053	0.085
	3	0.576	0.045	0.073
	1	0.574	0.047	0.076
	2	0.436	0.185	0.297
250	0	0.683	0.000	0.000
	4	0.599	0.084	0.123
	3	0.611	0.072	0.105
	1	0.648	0.035	0.052
	2	0.421	0.263	0.384
300	0	0.539	0.000	0.000
	4	0.489	0.050	0.094
	3	0.468	0.071	0.132
	1	0.507	0.032	0.059
	2	0.298	0.241	0.448
350	0	0.360	0.000	0.000
	4	0.337	0.024	0.066
	3	0.311	0.050	0.138
	1	0.341	0.019	0.054
	2	0.179	0.181	0.502
400	0	0.214	0.000	0.000
	4	0.207	0.007	0.034
	3	0.185	0.029	0.137
	1	0.211	0.004	0.018
	2	0.100	0.114	0.531

transmitted wave pack, extracted from the experimental raw data. Additionally, the amplitude variation between the welded and the non-welded plate was calculated for each frequency.

Hence, an amplitude-based DI was proposed as follows:

$$DI = |V_p - V_0|/V_0 \quad (2)$$

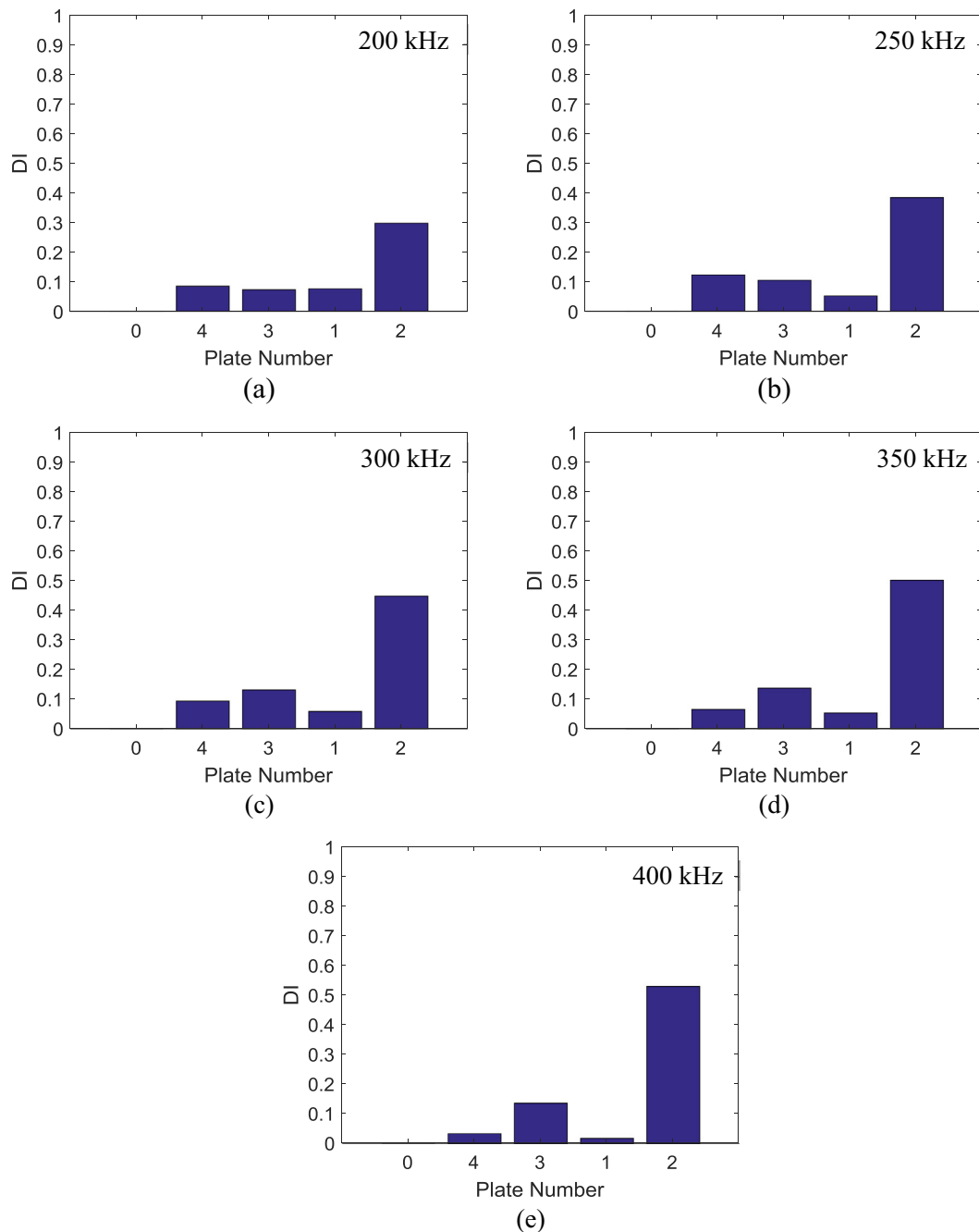
where  $V_p$  is the tested plate response signal amplitude and  $V_0$  is the Plate 0 (non-welded) response signal amplitude. Based on Eq. (2), the DIs were calculated for every excitation used and are presented in Table 2.

Fig. 12 presents the DI calculated for each plate after their excitation using the five frequencies tested in this study. The horizontal axes correspond to the plate number, and the vertical axes correspond to the calculated DI. The plates' numbers are presented in the ascending order of the CT scans' damage results (Section 3).

The five plots of the different frequencies (200, 250, 300, 350, and 400 kHz) show that the DI increases with increasing defect volume. Although some fluctuation in the DI values for Plates 1, 3, and 4 is observed, independently from the frequency, the largest DI is calculated for Plate 2, indicating the presence of the largest volume of defect in accordance with the CT scans results. Even though considerable precautions were taken in setting up the experiments (by controlling the position of the PZT wafers, the bond line, the wiring, and soldering), comparing signals from different plates might induce some variation. Moreover, the defects in Plates 1, 3, and 4 were close in size, resulting in a very small change in the signal amplitude that is in the noise level. Most importantly, to diminish the significant effect of the superposition of captured wave modes on the results, a mode separation technique was necessary.

## 7.2. Experimental and FEA results analysis using improved CEEMDAN technique

In this section, the mode separation of the Improved CEEMDAN technique was used to analyze the experimental and FEA wave propagation signals.



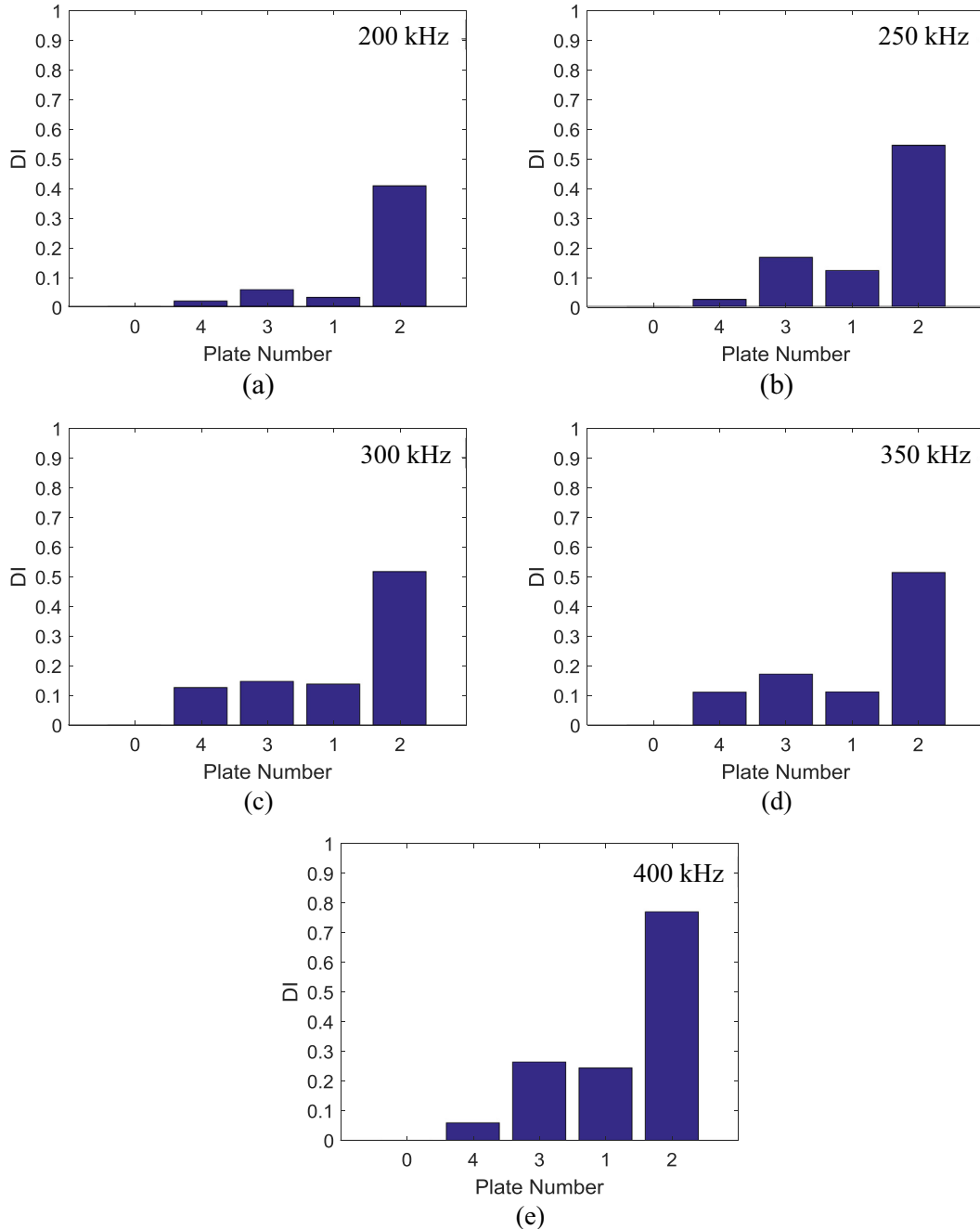
**Fig. 12.** DIs of the five specimens computed from the experimental responses before separation at (a) 200, (b) 250, (c) 300, (d) 350, and (e) 400 kHz.

The  $S_0$  mode was identified based on the group velocity and the correlation with the original signals. The amplitudes of the signals' wave fronts were acquired and the DIs were then calculated, using the methodology explained in the previous section, for each plate and for the five selected frequencies (200, 250, 300, 350, and 400 kHz).

The DI results of the experimental measurements are shown in Fig. 13. The evolutions of the DI results are consistent with the defect volumes measured by CT scans. The most severe damage is estimated for the welded Plate 2, as for all the tested frequencies the corresponding DI is the highest (0.388–0.77). Although an increase in the DI values with increasing damage severity is observed, Plate 1 and Plate 3 were inversely arranged, mainly due to similar weld quality. As mentioned earlier, even though significant precautions were taken in setting up the experiments, comparing signals from different plates may result in some variation. The difference between the signal responses of Plate 1 and Plate 3 ranged between 1% and 6% when

compared to the signal amplitude in the intact plate. As a matter of fact, any variation in the plate condition including adhesive quantity/thickness, PZT-plate bond quality, wiring and soldering, transducers' positions, plate dimensions and temperature and humidity conditions would lead to a small variation in the response signal. This variation may be in the order of the signal amplitude variation caused by a minor difference in the weld quality, as observed between Plate 1 and Plate 3. Moreover, the level of noise in the signals might be of the same order as the variations in the response due to the close-size defects.

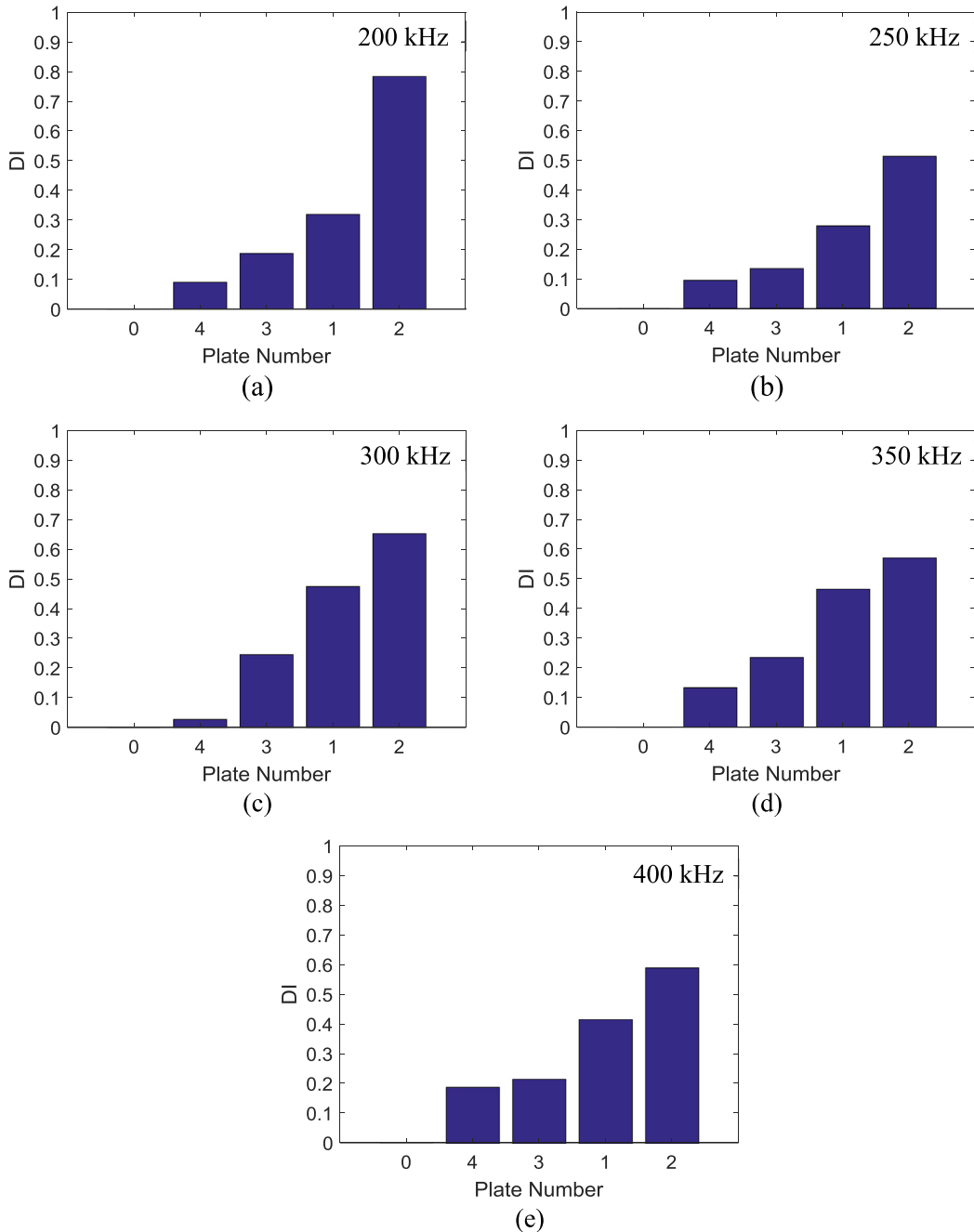
Another potential reason that can cause small variations, when comparing signals, is the superposition of the wave modes with the boundary reflections, that is attributed to the small dimensions of the specimens used. Using larger specimens would reduce the signal processing complexity and allow for a better convergence of the elastic wave modes [19]. However,



**Fig. 13.** DIs of the five specimens computed from the experimental responses after Improved CEEMDAN separation at (a) 200, (b) 250, (c) 300, (d) 350, and (e) 400 kHz.

the used specimen size was large enough for generating and collecting Lamb waves, as validated experimentally and using FEA. Furthermore, the 2% variation in the used separation technique (improved CEEMDAN), shown in Section 6, may also cause such variance.

Similarly, the  $S_0$  mode was separated from the FEA simulation results and analyzed. Fig. 14 shows the DIs calculated from the analyzed signals of the five different excitation frequencies applied to the five specimens. The classification according to the proposed DI is in complete agreement with the actual qualities of the welds. The consistency observed in the numerical results is mainly attributed to the elimination of several variables that could lead to the variation in the experimental results, including the placement and the wiring of the PZT wafers.

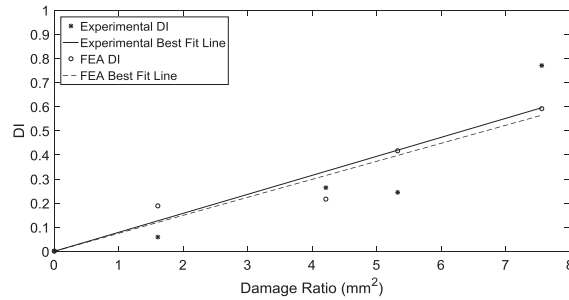


**Fig. 14.** DIs of the five specimens computed from the numerical responses after Improved CEEMDAN separation at (a) 200, (b) 250, (c) 300, (d) 350, and (e) 400 kHz.

**Table 3**

Damage volumes and damage ratios of the four damaged plates.

Plate number	$V_d$ = damage volume (mm <sup>3</sup> )	$R_d$ = $V_d$ /plate thickness (mm <sup>2</sup> )
4	43017	1.61
3	113.09	4.21
1	143.09	5.33
2	202.96	7.56

**Fig. 15.** Experimental and FEA DIs and their corresponding lines of best fit.

### 7.3. Assessment of the severity of damage

Subsequently, the damage volume in the welded region was correlated with the DI, to permit assessment of the severity of damage. A region of 30.5 mm (a multiple of the used pixel size) along the weld line and centered in the middle of the sensing path was considered to estimate the volume of damage ( $V_d$ ) from the “Mimics” models, as illustrated in Fig. 5. A separate mask was defined for the damage region under consideration for each of the plates. The volume of the mask was then estimated based on the voxel volumes. The resulting damage volumes for all the plates are summarized in Table 3, where the plates are arranged in ascending order based on the weld quality.

In fact, plate thickness plays an important role in the propagation behavior of a Lamb wave. Therefore, a generalized linear equation relating DI to damage severity is proposed in Eq. (3):

$$DI = a \times \frac{V_d}{\text{Plate Thickness}} = a \times R_d \quad (3)$$

where  $R_d$  is the damage ratio defined as  $V_d$  normalized by the thickness of the plate, and  $a$  is a constant.

The values of  $R_d$  were calculated and are summarized in Table 3.

The results for the DIs from both numerical and experimental signals, resulting from the excitation frequency of 400 kHz, were correlated with  $R_d$ . The scatter plots of the DIs as function of  $R_d$  are shown in Fig. 15. A linear regression passing through the origin is used to fit both the experimental and FEA data. The linear regression parameters were calculated using a “Matlab” built-in function, and the two lines are also shown in Fig. 15.

The equations for the experimental and FEA linear regressions were found to have good overlap and are described by:

$$\text{Experimental DI} = 0.0788 \times R_d \quad (4)$$

$$\text{FEA DI} = 0.0747 \times R_d \quad (5)$$

The R squared values of the linear fit for the experimental and FEA data were respectively 0.81 and 0.925, indicating high correlation between  $R_d$  and the proposed DI.

## 8. Conclusion

In this study, the capability of Lamb waves in detecting and quantifying worm holes in friction stir welded AZ31B magnesium alloy plates was demonstrated. Different weld qualities were obtained through control of the pin insertion depth. Piezoelectric wafers were used to excite and capture the fundamental symmetric  $S_0$  mode using different excitation frequencies. The “Improved CEEMDAN” method was applied to separate the  $S_0$  mode  $w$  from the captured signals. Further, a damage index was defined using the amplitude variation in the captured transmitted signals between the welded plates and the non-welded plate.

A new approach was proposed for constructing the finite element models of the welded plates based on CT scans using “Mimics” software. The finite element models could capture high level of detail in the welded region and the surface of the weld line.

The calculated damage indices based on the raw experimental data resulted in some inconsistency in the classification of the weld quality, variation that significantly improved after application of the “Improved CEEMDAN” technique. On the other hand, the damage indices, computed based on the finite element analysis, provide the correct classification of the welds in correlation with the CT scanning.

3D (CT scan based) models were used to calculate the damage volumes in the welded regions and to determine correlation with the damage indices that were obtained from the experimental and numerical data at an excitation frequency of 400 kHz.

In conclusion, Lamb waves demonstrated high sensitivity to the presence of defects in FSW, and the suggested methodology appears promising for use in the assessment of welded components.

## Acknowledgments

Recognition and gratitude are addressed to the Lebanese National Council for Scientific Research (CNRS) for their Award #103085. The financial support of the University Research Board at the American University of Beirut for their Award #103008 is also acknowledged. The authors thank Dr. Nayla Cortas and Ms. Salam Al Hamra at the American University of Beirut – Medical Center (AUBMC) for their help in performing the needed CT scans.

## Appendix A.

### i. Necessary definitions

- $R_k$ : is the  $k^{\text{th}}$  residue of decomposition.
- $\bar{R}_k$ : is the local mean of  $R_k$ .
- $E_k(R_k)$ : is the  $k^{\text{th}}$  mode of  $R_k$  obtained by EMD.
- $N^{(i)}$ : is the  $i^{\text{th}}$  realization of a white Gaussian noise with zero mean and unit variance.
- SNR: is the desired signal to noise ratio between the first added noise and the original signal.

### ii. EMD algorithm

- 1) Set  $k = 0$  and  $R_0 = s$ ; where  $s$  is the signal to be decomposed by EMD.
- 2) Find all the extrema of  $R_k$ .
- 3) Interpolate among the extrema of  $R_k$  to obtain the lower and upper envelopes  $e_{\min}$  and  $e_{\max}$ .
- 4)  $\bar{R}_k = (e_{\min} + e_{\max})/2$ .
- 5)  $I_{k+1} = R_k - \bar{R}_k$ .
- 6) If  $I_{k+1}$  is an IMF, then:
  - $E_{k+1}(s) = I_{k+1}$ .
  - $R_{k+1} = s - \sum_{i=1}^{k+1} E_i(s)$
  - $k = k + 1$ .
  - Go to step 2.
  - Else:
    - $R_k = I_{k+1}$
    - Go to step 2.

The loop continues until  $R_k$  fulfills a predefined stopping condition (for instance,  $R_k$  becomes monotonic)

### iii. Improved CEEMDAN algorithm:

- 1) Set  $k = 0$  and  $R_0 = s$ ; where  $s$  is the signal to be decomposed by Improved CEEMDAN.
- 2) Compute using EMD the local means of  $I$  realizations of  $R_k$ :

$$R_k^{(i)} = R_k + \alpha_k E_{k+1}(N^{(i)})$$

where:

$$\alpha_k = \begin{cases} \varepsilon_0 \cdot \frac{\text{std}(R_0)}{\text{std}(E_1(N^{(i)}))} & \text{for } k = 0 \\ \varepsilon_0 \cdot \text{std}(R_k) & \text{for } k \geq 1 \end{cases}$$

and:

$$\varepsilon_0 = \frac{1}{\text{SNR}}$$

$$3) \mu_k = \text{Average}(\bar{R}_k^{(i)}) = \frac{1}{I} \sum_{i=1}^I \bar{R}_k^{(i)}$$

$$4) k = k + 1$$

$$5) \text{The } k^{\text{th}} \text{ mode: } M_k = R_{k-1} - \mu_{k-1}.$$

$$6) \text{The } k^{\text{th}} \text{ residue: } R_k = R_{k-1} - M_k = \mu_{k-1}.$$

$$7) \text{Go to step 2.}$$

The loop continues until  $R_k$  fulfills a predefined stopping condition (for instance,  $R_k$  becomes monotonic).

## References

- [1] A.S. Babu, C. Devanathan, An overview of friction stir welding, *Int. J. Res. Mech. Eng. Technol.* 3 (2013) 259–265.
- [2] W. Thomas, E. Nicholas, J.C. Needham, M. Murch, P. Temple-Smith, C. Dawes, Friction stir welding, in: *International Patent Application no. PCT/GB92102203 and Great Britain Patent Application*, 1991.
- [3] W. Thomas, M. Murch, E. Nicholas, P. Temple-Smith, J. Needham, C. Dawes, Improvements relating to friction welding, *Patent Number EP 0653265*, 1995.
- [4] M. Muthukrishnan, K. Marimuthu, Some studies on mechanical properties of friction stir butt welded Al-6082-T6 plates, *Frontiers Automobile Mech. Eng. (FAME) 2010 (2010)* 269–273.
- [5] Y.-H. Zhao, S.-B. Lin, L. Wu, F.-X. Qu, The influence of pin geometry on bonding and mechanical properties in friction stir weld 2014 Al alloy, *Mater. Lett.* 59 (2005) 2948–2952.
- [6] N. Kumbhar, K. Bhanumurthy, Friction stir welding of Al 6061 alloy, *Asian J. Exp. Sci.* 22 (2008) 63–74.
- [7] H.A. Kumar, V.V. Ramana, An overview of friction stir welding (FSW): A new perspective, *Research Inventy: Int. J. Eng. Sci.* 4 (2014) 01–04.
- [8] A. Ammouri, A. Kheireddine, G. Kridli, R. Hamade, FEM optimization of process parameters and in-process cooling in the friction stir processing of magnesium alloy AZ31B, in: *ASME 2013 International Mechanical Engineering Congress and Exposition*, 2013, pp. V02AT02A079–V02AT02A079.
- [9] A. Ammouri, R. Hamade, On the selection of constitutive equation for modeling the friction stir processes of twin roll cast wrought AZ31B, *Mater. Design* 57 (2014) 673–688.
- [10] A.H. Ammouri, R.F. Hamade, Comparison of material flow stress models toward more realistic simulations of friction stir processes of Mg AZ31B, *Adv. Mater. Res.* (2014) 18–22.
- [11] A.H. Ammouri, A.H. Kheireddine, R.F. Hamade, A numerical model for predicting the Zener-Hollomon parameter in the friction stir processing of AZ31B, *Mater. Sci. Forum* (2014) 93–99.
- [12] A. Kheireddine, A. Ammouri, G. Kridli, R. Hamade, Experimentally validated thermo-mechanically coupled FE simulations of Al/Mg friction stir welded joints, in: *ASME 2013 International Mechanical Engineering Congress and Exposition*, 2013, pp. V02BT02A008–V02BT02A008.
- [13] Z. El Chlouk, G. Ayoub, G. Kridli, R. Hamade, Intermetallic compound formation in Al/Mg friction stir welded (FSW) butt joints, in: *ASME 2014 International Mechanical Engineering Congress and Exposition*, 2014, pp. V014T11A010–V014T11A010.
- [14] W.J. Arbegast, Friction stir joining: characteristic defects, *South Dakota School Mines Technol.* (2003).
- [15] W. Ostachowicz, P. Kudela, M. Krawczuk, A. Zak, I. Books24x, *Guided Waves in Structures for SHM: The Time - domain Spectral Element Method vol. 1*. Hoboken: Wiley, 2011.
- [16] Z. Su, L. Ye, Y. Lu, Guided lamb waves for identification of damage in composite structures: A review, *J. Sound Vibration* 295 (2006) 753–780.
- [17] C.-T. Ng, M. Veidt, A lamb-wave-based technique for damage detection in composite laminates, *Smart Mater. Struct.* 18 (2009) 074006.
- [18] V.T. Rathod, D. Roy, Mahapatra, Ultrasonic Lamb wave based monitoring of corrosion type of damage in plate using a circular array of piezoelectric transducers, *NDT and E Int.* 44 (2011) 628–636.
- [19] S. Mustapha, L. Ye, D. Wang, Y. Lu, Debonding detection in composite sandwich structures based on guided waves, *AIAA J.* 50 (2012) 1697–1706.
- [20] C.-T. Ng, M. Veidt, Scattering characteristics of lamb waves from debondings at structural features in composite laminates, *J. Acoust. Soc. Am.* 132 (2012) 115–123.
- [21] A. Bagheri, K. Li, P. Rizzo, Reference-free damage detection by means of wavelet transform and empirical mode decomposition applied to Lamb waves, *J. Intelligent Mater. Syst. Struct.* 24 (2013) 194–208.
- [22] S. Mustapha, L. Ye, Propagation behaviour of guided waves in tapered sandwich structures and debonding identification using time reversal, *Wave Motion* 57 (2015) 154–170.
- [23] S. Mustapha, L. Ye, X. Dong, M.M. Alamdari, Evaluation of barely visible indentation damage (BVID) in CF/EP sandwich composites using guided wave signals, *Mech. Syst. Signal Process* 76–77 (2016) 497–517.
- [24] M.A. Fakhri, S. Mustapha, M. Makki Alamdari, L. Ye, Symbolic dynamics time series analysis for assessment of barely visible indentation damage in composite sandwich structures based on guided waves, *J. Compos. Mater.* (2017), 0021998317696138.
- [25] S. Burch, N. Bealing, A physical approach to the automated ultrasonic characterization of buried weld defects in ferritic steel, *NDT Int.* 19 (1986) 145–153.
- [26] M. Karim, M. Awal, T. Kundu, Elastic wave scattering by cracks and inclusions in plates: in-plane case, *Int. J. Solids Struct.* 29 (1992) 2355–2367.
- [27] S. Dixon, C. Edwards, S.B. Palmer, A laser-EMAT system for ultrasonic weld inspection, *Ultrasonics* 37 (1999) 273–281.
- [28] R. Kažys, L. Mažeika, R. Barauskas, R. Raišutis, V. Cicėnas, A. Demčenko, 3D analysis of interaction of Lamb waves with defects in loaded steel plates, *Ultrasonics* 44 (2006) e1127–e1130.
- [29] M. Arone, D. Cerniglia, V. Nigrelli, Defect characterization in Al welded joints by non-contact Lamb wave technique, *J. Mater. Process. Technol.* 176 (2006) 95–101.
- [30] M. Lu, X. Lu, L. Zhou, Z. Su, L. Ye, Guided-wave-based detections of weld and crack in steel plates, *Second International Conference on Smart Materials and Nanotechnology in Engineering*, 2009, 749325–749325-8.
- [31] J. Yang, J. He, X. Guan, D. Wang, H. Chen, W. Zhang, et al, A probabilistic crack size quantification method using in-situ Lamb wave test and Bayesian updating, *Mech. Syst. Signal Process.* 78 (2016) 118–133.
- [32] Ó. Martín, M. Pereda, J.I. Santos, J.M. Galán, Assessment of resistance spot welding quality based on ultrasonic testing and tree-based techniques, *J. Mater. Process. Technol.* 214 (2014) 2478–2487.
- [33] J. Liu, G. Xu, X. Gu, G. Zhou, Ultrasonic test of resistance spot welds based on wavelet package analysis, *Ultrasonics* 56 (2015) 557–565.
- [34] J. Santos, M. Santos, Lamb waves technique applied to the characterization of defects in friction stir welding of aluminum plates: comparison with X-ray and ultrasonic C-scan, *J. Testing Evaluation* 38 (2010) 1–6.
- [35] S. Delrue, M. Tabatabaeipour, J. Hettler, K. Van Den Abeele, Applying a nonlinear, pitch-catch, ultrasonic technique for the detection of kissing bonds in friction stir welds, *Ultrasonics* 68 (2016) 71–79.
- [36] M. Tabatabaeipour, J. Hettler, S. Delrue, K. Van Den Abeele, Non-destructive ultrasonic examination of root defects in friction stir welded butt-joints, *NDT & E Int.* 80 (2016) 23–34.
- [37] A. Dorbane, G. Ayoub, B. Mansoor, R. Hamade, G. Kridli, R. Shabadi, et al, Microstructural observations and tensile fracture behavior of FSW twin roll cast AZ31 Mg sheets, *Mater. Sci. Eng.: A* 649 (2016) 190–200.
- [38] N. Afrin, D. Chen, X. Cao, M. Jahazi, Strain hardening behavior of a friction stir welded magnesium alloy, *Scripta Mater.* 57 (2007) 1004–1007.
- [39] Q. Nguyen, M. Gupta, Increasing significantly the failure strain and work of fracture of solidification processed AZ31B using nano-Al<sub>2</sub>O<sub>3</sub> particulates, *J. Alloys Compd.* 459 (2008) 244–250.
- [40] H. Palaniswamy, G. Ngaile, T. Altan, Finite element simulation of magnesium alloy sheet forming at elevated temperatures, *J. Mater. Process. Technol.* 146 (2004) 52–60.
- [41] S. Mustapha, L. Ye, Leaky and non-leaky behaviours of guided waves in CF/EP sandwich structures, *Wave Motion* 51 (2014) 905–918.
- [42] WAVESCOPE: Dispersion curves, group velocities and tuning for metallic structures, *Laboratory for Active Materials and Smart Structures (LAMSS)*.
- [43] C.-T. Ng, On the selection of advanced signal processing techniques for guided wave damage identification using a statistical approach, *Eng. Struct.* 67 (2014) 50–60.
- [44] N.E. Huang, Z. Shen, S.R. Long, M.C. Wu, H.H. Shih, Q. Zheng, et al, The empirical mode decomposition and the Hilbert spectrum for nonlinear and non-stationary time series analysis, in: *Proceedings of the Royal Society of London A: Mathematical, Physical and Engineering Sciences*, 1998, pp. 903–995.
- [45] A. Raghavan, C.E. Cesnik, Guided-wave signal processing using chirplet matching pursuits and mode correlation for structural health monitoring, *Smart Mater. Struct.* 16 (2007) 355.

- [46] M.A. Colominas, G. Schlotthauer, M.E. Torres, Improved complete ensemble EMD: A suitable tool for biomedical signal processing, *Biomed. Signal Process. Control* 14 (2014) 19–29.
- [47] Z. Wu, N.E. Huang, Ensemble empirical mode decomposition: a noise-assisted data analysis method, *Adv. Adaptive Data Anal.* 1 (2009) 1–41.
- [48] J.-R. Yeh, J.-S. Shieh, N.E. Huang, Complementary ensemble empirical mode decomposition: A novel noise enhanced data analysis method, *Adv. Adaptive Data Anal.* 2 (2010) 135–156.
- [49] M.E. Torres, M.A. Colominas, G. Schlotthauer, P. Flandrin, A complete ensemble empirical mode decomposition with adaptive noise, in: *Acoustics, Speech and Signal Processing (ICASSP)*, 2011 IEEE International Conference on, 2011, pp. 4144–4147.
- [50] Z. Peng, W.T. Peter, F. Chu, A comparison study of improved Hilbert–Huang transform and wavelet transform: application to fault diagnosis for rolling bearing, *Mech. Syst. Signal Process.* 19 (2005) 974–988.
- [51] A. Ayenu-Prah, N. Attoh-Okine, A criterion for selecting relevant intrinsic mode functions in empirical mode decomposition, *Adv. Adaptive Data Anal.* 2 (2010) 1–24.